

Sensitivity of multi-detector hybrid statistic in CBC search

K. Haris,^{1,*} Vinaya Valsan,^{1,†} and Archana Pai^{1,‡}

¹*Indian Institute of Science Education and Research Thiruvananthapuram,
Computer Science Building, College of Engineering Campus,
Trivandrum, Kerala, 695016, India*

(Dated: June 3, 2022)

Abstract

In this paper we compare the performance of two likelihood ratio based detection statistics namely maximum likelihood ratio statistic and *hybrid* statistic in the context of multi-detector coherent gravitational wave search for the compact binary coalescence in various 2, 3, 4 and 5 detector networks. We perform simulations for non-spinning neutron star - black hole binary injections distribution in a distance range 100Mpc - 1200Mpc uniform in volume. We observe that, on average, the maximum likelihood ratio statistic recover $\sim 35.29\%$, 50.78% , 62.37% and 70.66% of injections in 2, 3, 4 and 5 detector networks respectively for a fixed false alarm probability of 10^{-7} . Further, we note that, compared to the maximum likelihood ratio statistic, the *hybrid* statistic recover $\sim 7.35\%$, $\sim 4.48\%$, $\sim 2.5\%$ and $\sim 1.19\%$ more injection in 2, 3, 4 and 5 detector networks respectively for the same false alarm probability.

PACS numbers: 04.80.Nn, 07.05.Kf, 95.55.Ym

arXiv:1701.03952v1 [astro-ph.IM] 14 Jan 2017

*Electronic address: haris@iisertvm.ac.in

†Electronic address: vinayavalsan2010@iisertvm.ac.in

‡Electronic address: archana@iisertvm.ac.in

I. INTRODUCTION

Detection of gravitational waves (GW) from two binary black hole mergers [1, 2] by Advanced LIGO detectors has opened a new observational window to our universe. Addition of more advanced interferometers like Virgo [3, 4], KAGRA [5, 6] and LIGO-India [7, 8] located in different continents will provide additional information like source location and polarization of incoming gravitational wave signal. Gravitational waves from inspiraling compact binary coalescences (CBC) composed of neutron stars (NS) and black holes (BH) are primary sources for multi-detector interferometric GW networks. Based on LIGO's initial observations, it is expected that the Advanced LIGO detectors could observe tens of NS-NS and NS-BH merger events per year along with hundreds of binary black hole mergers once they achieve their designed sensitivity by 2019 [9–12].

The coherent detection schemes for the GW search of CBC sources with known source location (targeted search) has been developed in literature by various groups [13–15]. The coherent searches are carried out by constructing a two stream maximum likelihood ratio (MLR) statistic by combining data from different detectors in a phase coherent fashion. The coherent scheme has been implemented in the GW follow-up search of gamma ray bursts (GRBs) observed by the Inter Planetary Network (IPN) satellites, where the source location is known a priori from IPN data [16, 17]. Further, in [18] the authors have implemented all sky coherent search scheme for LIGO network as an extension of MLR based targeted coherent analysis by putting templates in the sky coordinates.

Motivated from the study of statistical properties of MLR statistic, in [19], authors developed a new *hybrid* statistic for the coherent search of CBC sources. The work clearly demonstrates (both analytically and numerically) that the *hybrid* statistic can recover more CBC events compared to the MLR statistic for a given type of source (due to the increased distance reach). In this work, we carry out extensive performance comparison of MLR statistic and the *hybrid* statistic in different networks with 2,3,4 and 5 detector combinations for NS-BH source arbitrarily located as well as oriented in the sky in a given distance range (100Mpc - 1200Mpc) uniform in volume. We demonstrate that the *hybrid* statistic gives $\sim 7.35\%$, $\sim 4.48\%$, $\sim 2.5\%$ and $\sim 1.19\%$ relative improvement in the injection recovery rate over MLR statistic for 2, 3, 4 and 5 detector networks respectively for a fixed false alarm probability (FAP) of 10^{-7} . Further we note that this improvement in injection recovery varies with the inclination angle of binary injections. As expected the *hybrid* statistic gives best performance for near face-on/off injections and gives worst performance for near edge-on injections.

The paper is organized as follows. Section II gives an overview of the global network of interferometers. The properties of various multi-detector networks are discussed in Section III. In Section IV, we briefly discuss the two detection statistics used for multi-detector search of CBC signals namely MLR statistic and *hybrid* statistic. In Section V, we carry out numerical simulations to estimate detection efficiency of MLR statistic as well as *hybrid* statistic for various networks. Finally, in Section VI, we summarize the results.

II. GROUND BASED GW MULTI-DETECTOR NETWORK

A global network of ground based advanced optical laser interferometric detectors has been taking shape. The 4 km arm-length twin Advanced LIGO detectors are located at Hanford (H) and Livingston (L) in the USA [20–23]. The first observation run of Advanced

LIGO detectors took place for a period of four months starting from September 2015. During the run, the LIGO detectors made the historical detection of GW from two binary BH mergers namely GW150914 (Sept.14, 2015) and GW151226 (Dec.26, 2015) [1, 2, 24]. The up-gradation of $3km$ Virgo (French-Italian) detector (V) located in Pisa, Italy is ongoing [3, 4]. The Japanese cryogenic detector KAGRA (K) located in Kamioka Observatory, Gifu is a $3km$ detector with operating temperature $\sim 20K$ [5, 6]. KARGA is expected to join the global network within a decade. The proposal for setting up a $4km$ LIGO detector in India (I)¹ as an extension of LIGO network has received the approval [7, 8]. These five advanced interferometric detectors will together form a ground based km arm-length Michelson type (with perpendicular arms) 5-detector network. The orientations and locations of the detectors are taken from Table 1 of [25].

For a global multi-detector network with independent noises, the network signal to noise ratio (SNR) square ρ^2 is the sum of the individual SNR squares and is given by

$$\rho^2 = \sum_m \rho_m^2 \equiv \sum_m F_{+m}^2(\mathbf{h}_+|\mathbf{h}_+) + F_{\times m}^2(\mathbf{h}_\times|\mathbf{h}_\times). \quad (2.1)$$

Here, $F_{+m}, F_{\times m}$ are the antenna pattern functions of m -th detector, which give the direction response of individual detector (For detailed expressions, See Eq.(7) of [15]). $F_{+m}(\theta, \phi), F_{\times m}(\theta, \phi)$ are functions of binary source location (θ, ϕ) and the orientation of the detectors with respect to the Earth. The $\tilde{h}_+(f), \tilde{h}_\times(f)$ are the two polarizations of GW in Einstein's gravity².

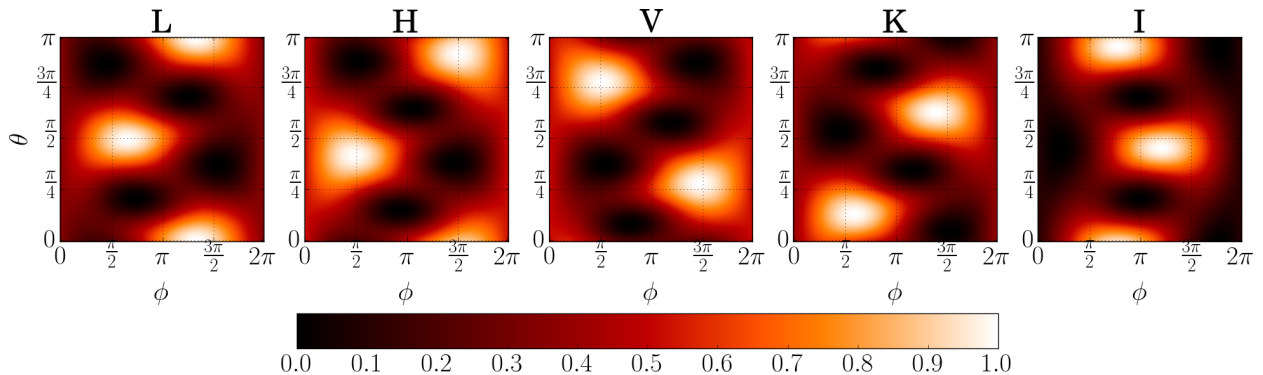


FIG. 1: Sky map of antenna pattern function ($F_+^2 + F_\times^2$) for individual detectors. Each interferometer has 2 maxima along the local zenith and beneath and four blind directions along the perpendicular bisectors of the interferometer arms denoted by the dark patches.

In Figure 1, we draw the sky maps for the individual detectors. The antenna pattern for each of the GW interferometers is quadrupolar in nature with 2 maxima (along the local zenith and beneath) and 4 blind directions in the plane of the interferometer (directions along the bisectors of arms). Due to distinct geographical locations, naturally the plane of each of these detectors are distinct and hence the maximum response and the blind directions as well (See Fig 1). Please note that the two maxima of the detector V overlap with the

¹ In this study, we take Pune, India as the location for the detector in India.

² The scalar product $(\mathbf{a}|\mathbf{b})_m = 4\Re \int_0^\infty \tilde{a}(f) \tilde{b}^*(f) df$, where $\tilde{a}(f) = \tilde{a}(f)/S_n(f)$ is the over-whitened version of frequency series $\tilde{a}(f)$ with $S_n(f)$ as the one-sided noise power spectral density (PSD) of m -th detector.

two distinct blind spots of L and H respectively filling the blind directions. Thus, we expect that, when more detectors start taking the data together, more sky becomes visible to the multi-detector network as a whole. Further, with improved visibility, the network sees much deeper in space.

III. MULTI-DETECTOR SKY COVERAGE, MAXIMUM DISTANCE REACH AND THE FRACTIONAL DETECTION VOLUME

Below, we define the sky coverage as well the maximum distance reach (R_h) for different networks. The sky coverage and R_h would depend on the binary inclination. However, it can be shown that the network SNR square averaged over the binary inclination angle ϵ and the polarization angle Ψ gives

$$\langle \rho^2 \rangle_{\epsilon, \Psi} = \frac{14}{15} \sum_m F_{+m}^2 + \frac{2}{3} \sum_m F_{\times m}^2 \sim \sum_m F_{+m}^2 + \sum_m F_{\times m}^2. \quad (3.1)$$

This is very similar to the face-on case ($\epsilon = 0$). Hence, we carry out the sky coverage as well as distance reach exercise for the face-on case. The results would be same as if we take average over the binary orientations. Hence in [25], the author term R_h as the *mean horizon distance*.

Further, the multi-detector network covers different distance in different directions. The fractional detection volume \mathcal{V} , following [25], measures the 3 dimensional detectable sky volume of a given network.

Sky Coverage: The isotropy in directional response of a multi-detector network can be quantified in terms of sky coverage – the percentage of sky area *visible* to a multi-detector network. Following [25], we define the sky coverage as the sky area with the network SNR ρ greater than $1/\sqrt{2}$ of the maximum directional SNR.

Maximum distance reach: The maximum distance observed by a network in the most sensitive direction for a given source. This is determined by the choice of threshold SNR ρ_{th} .

Fractional sky volume \mathcal{V} : For a given network with the threshold network SNR of ρ_{th} , we define

$$\mathcal{V} = \int_0^R \int_0^\pi \int_0^{2\pi} r^2 \sin \theta \, dr \, d\theta \, d\phi. \quad (3.2)$$

Here, $R(\theta, \phi, \rho_{th})$ is a distance reach of a network in the given direction. In fact, R_h is a maximum of $R(\theta, \phi, \rho_{th})$.

Figure 2 shows the directional SNR for various 2, 3, 4 and 5 detector networks with LIGO Hanford (H), LIGO Livingston (L), Virgo (V), KAGRA (K) and LIGO India (I). For this exercise, we assume all detectors to have "zero-detuning, high power" Advanced LIGO noise PSD [26]. We consider the source to be face-on non-spinning NS-BH with masses $(2.0 - 10)M_\odot$ located at 500 Mpc.

Broadly we can see that, with more number of detectors, more and more sky becomes brighter, *i.e.*, sensitive to a network. This sensitivity would in turn translate into the distance reach of a network. The Table I gives the sky coverage (Column III) and maximum distance reach (Column IV) of all possible 2 - 5 detector combinations. For the maximum distance reach we take the threshold SNR $\rho_{th} = 8$. The same is represented graphically in the Figure 3, where one can clearly see the trend and compare the numbers. To understand the

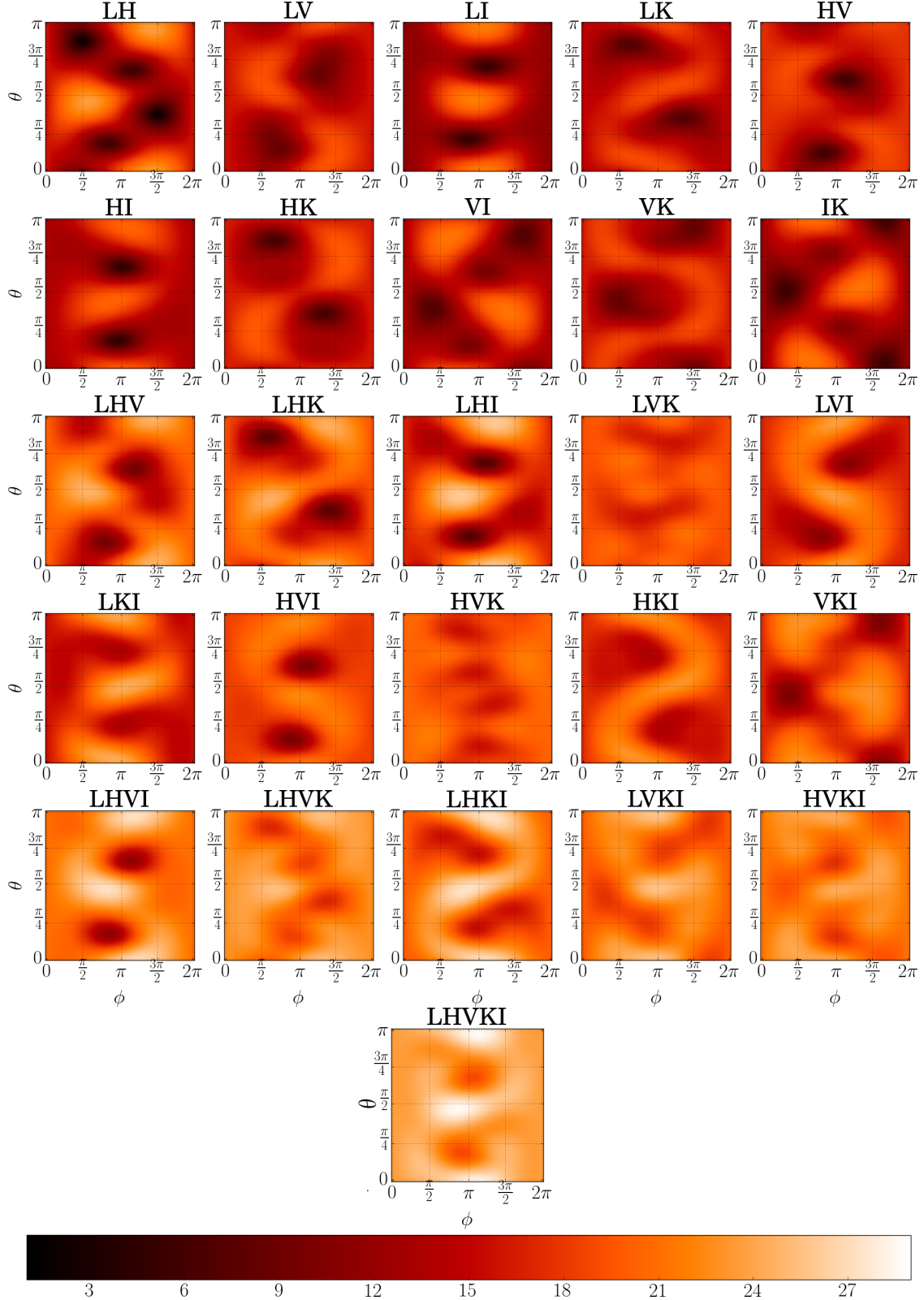


FIG. 2: Sky map of network SNR ρ of inspiral signal with masses $(2 - 10)M_{\odot}$, inclination angle $\epsilon = 0$, polarization angle $\Psi = 0$, and distance $r = 500\text{Mpc}$ for various 2, 3, 4 and 5 detector network configurations. We assume all the detectors with "zero-detuning, high power" Advanced LIGO noise curve [26].

sky-coverage as well as the maximum distance reach R_h between various combinations, one should focus on the relative orientation between the pairs of detectors in the given network.

We define the angle between the two detector (i and j) planes (or local zenith) as δ_{ij} . This angle is tabulated for different detector pairs in Table I (Column II in bracket). Using this we define a geometrical quantity

$$\mathcal{G} \equiv \sqrt{I[1 + (I - 1) \langle \cos \delta_{ij} \rangle]^{1/2}}, \quad (3.3)$$

where I is the number of detectors in a network. The $\langle \cdot \rangle$ denotes average over all possible ${}^I C_2$ pairs of detectors in the network. This quantity represents the magnitude of sum of unit vectors along the axis of the antenna patterns of the detectors in the network. Please note, when all the detectors in a network are aligned, $\mathcal{G} = I$. This would translate into low sky coverage and large maximum distance reach R_h . We explain the sky coverage and R_h of different networks using this quantity computed for each network tabulated in Table I (Column II).

Two detectors: For two detector networks, the $\mathcal{G} = \sqrt{2(1 + \cos \delta)}$ – depends on the angle between the detector planes. Thus, the sky-coverage increases with increase in the δ (See the trend in sky coverage). Further, we see the decrease in R_h as the angle between the two planes increases. This can be natural, as for the nearly aligned detectors (*i.e.* low δ , e.g. LH), the distance reach would be highest along the most sensitive direction. However, the δ for VK pair is maximum, in fact the V and K planes are almost orthogonal. This in turn gives close to the least maximum distance reach amongst all the 2 detector networks. Please note that LK and HV show slightly higher sky coverage compared to VK in spite of lower δ . This can be attributed to the in-plane orientation of the detectors. In summary; amongst the 2 detector networks HV (LH) gives maximum (minimum) sky coverage and LH (LK) gives the maximum (minimum) maximum distance reach.

Three detectors: We note that with increase in the sky coverage, the maximum distance reach decreases. Please note that for a 3 detector network $\sqrt{3} \leq \mathcal{G} \leq 3$ with $\sqrt{3}$ correspond to detectors with antenna-patterns forming an orthogonal triplet. We note that HVK and LVK combinations give maximum sky coverage (100%) and minimum R_h (1.36Gpc, 1.32Gpc), which attributes to \mathcal{G} closer to the lower end of the spectrum. The combination LHI gives minimum sky coverage (47.02%) and maximum R_h (1.63Gpc), which attributes to the higher value of \mathcal{G} (close to 3). Please note LKI, LHV and LHK show similar sky coverage and maximum distance reach R_h .

Four detectors: The networks LHVK, LVKI and HVKI show sky coverage very close to 100%. The 4 detector networks with L, H and I together show slightly low sky coverage as L, H and I show good alignment. The trend in the distance reach is reverse to that of the sky coverage.

Five detectors: The 5 detector gives the maximum distance reach of 1.80Gpc almost 1.22 times deeper than the two detector LH and 1.51 times deeper than LK.

In Table I (Column V), we tabulate the fractional detection volume for each network as compared with the single LIGO-L detector. The trends are exactly similar to the maximum distance reach R_h . This is expected as higher is the distance reach, larger is the detection volume expected to cover. Thus, from this exercise, the 5 detector LHVKI covers sky volume 3.5 times that of LH and 3.8 times that of LK. This would translate into the injection recovery with these networks which we will discuss in the following section.

For NS-NS system, the sky coverage would remain the same. However, the distance reach would scale by a factor $\sim \mathcal{M}_c^{5/6}$ and the absolute detection volume would scale as $\sim \mathcal{M}_c^{5/2}$,

where \mathcal{M}_c is the *chirp mass* of the system. Here, we assume that the noise PSDs in each detector are identical. However, with real advanced detector noise curves, there would be small variations in the above estimates.

Network	$\mathcal{G}(\delta \text{ in deg.})$	Sky Coverage	R_h in Gpc	$\mathcal{V}/\mathcal{V}_L$
LH	1.94 (27.25)	34.38%	1.48	2.77
LI	1.8 (51.76)	42.48%	1.37	2.65
KI	1.75 (57.46)	45.39%	1.34	2.62
VI	1.75 (57.99)	46.28%	1.34	2.63
HI	1.67 (66.67)	58.85%	1.28	2.59
HK	1.61 (72.56)	63.29%	1.24	2.57
LV	1.57 (76.76)	66.8%	1.22	2.57
VK	1.46 (86.62)	71.08%	1.19	2.55
LK	1.52 (80.56)	73.5%	1.19	2.56
HV	1.54 (79.63)	75.06%	1.20	2.56
LHI	2.61	47.02%	1.63	4.81
LKI	2.37	61.91%	1.53	4.65
LHV	2.36	62.09%	1.55	4.72
LHK	2.39	63.68%	1.54	4.73
LVI	2.40	69.72%	1.48	4.67
HKI	2.34	70.75%	1.44	4.63
VKI	2.30	81.39%	1.44	4.65
HVI	2.28	84.28%	1.40	4.62
HVK	2.02	100.0%	1.36	4.53
LVK	1.97	100.0%	1.32	4.51
LHKI	3.12	68.89%	1.72	7.16
LHVI	3.07	79.44%	1.71	7.14
LHVK	2.76	96.47%	1.59	7.0
LVKI	2.88	97.25%	1.61	7.01
HVKI	2.82	100.0%	1.52	6.96
LHVKI	3.58	95.09%	1.80	9.77

TABLE I: \mathcal{G} , Sky Coverage, Maximum distance reach R_h in Gpc and the fractional detection volume with respect to single detector L for all possible 2-5 network configurations. We choose the $\rho_{th} = 8$ for the typical NS-BH system with masses $(2 - 10)M_\odot$.

IV. MULTI-DETECTOR CBC SEARCH: MLR VS HYBRID STATISTIC

The targeted coherent search of CBC in Gaussian noise with a network of detectors is generally carried out by using the maximum likelihood ratio (MLR) approach \mathcal{L} [13–15]. The multi-detector MLR statistic \mathcal{L} (maximized the likelihood ratio over constant amplitude A , binary inclination angle ϵ , polarization angle Ψ and the initial phase of the signal ϕ_0) can be expressed in terms of two effective synthetic data streams obtained by linearly combining

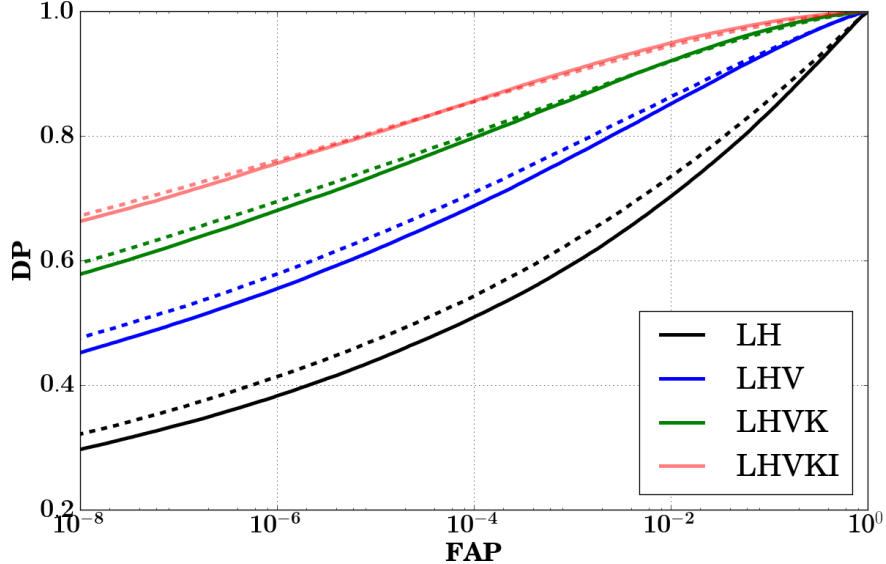


FIG. 4: ROC curves of \mathcal{L} (solid curve) and \mathcal{L}^{mx} (dashed curve) for networks LH, LHV, LHVK and LHVKI. The NS-BH binary with masses $(2 - 10)M_{\odot}$ is distributed uniformly over the sky with source distance sampled uniformly in volume between $(100 - 1200)\text{Mpc}$. The binary orientation $\cos \epsilon$ and Ψ are uniformly sampled from the ranges $(-1, 1)$ and $(0, 360^{\circ})$ respectively. All detectors are assumed with "zero-detuning, high power" Advanced LIGO PSD [26] noise curve.

with

$$\mathcal{L}^{0,\pi} = \langle \mathbf{z}^{0,\pi} | \mathbf{h}_0 \rangle^2 + \langle \mathbf{z}^{0,\pi} | \mathbf{h}_{\pi/2} \rangle^2 . \quad (4.4)$$

Here the synthetic streams,

$$\tilde{z}^0(f) \equiv \sum_m \frac{\mathbf{F}_m}{\|\mathbf{F}'\|} \tilde{x}_m(f), \quad \tilde{z}^{\pi}(f) \equiv \sum_m \frac{\mathbf{F}_m^*}{\|\mathbf{F}'\|} \tilde{x}_m(f). \quad (4.5)$$

In contrast with the two stream multi-detector MLR statistic, the single stream *hybrid* statistic gives less FAP with little compromise on detection probability (DP). In [19], using the Receiver Operator Characteristic (ROC) curves, the authors demonstrated that the *hybrid* statistic gives better performance compared to the MLR statistic for a wide range of binary inclination angle ($\epsilon < 70^{\circ}$ and $\epsilon > 110^{\circ}$).

V. PERFORMANCE COMPARISON BETWEEN \mathcal{L} AND \mathcal{L}^{mx}

In this section, we carry out numerical simulations to estimate the detection performance of \mathcal{L}^{mx} and \mathcal{L} for all combinations of 2, 3, 4 and 5 detector networks composed of L, H, V, K, and I. For this exercise, we distribute non-spinning NS-BH systems with masses $(2 - 10)M_{\odot}$ over the sky in the distance range $(100 - 1200)\text{Mpc}$ uniform in volume. The samples involve uniform sampling of $\cos \epsilon$ and Ψ from the ranges $(-1, 1)$ and $(0, 360^{\circ})$ respectively. The total number of sampled points are 5×10^5 with we denote by sample-1. The subset of them belong to $(\epsilon \leq 70^{\circ} \text{ or } \epsilon \geq 110^{\circ})$ with number of samples 3.3×10^5 and is denoted by sample-2.

All the detectors are assumed to have Gaussian, random noise with the noise PSD following "zero-detuning, high power" Advanced LIGO noise curve [26]. However, since the

FAP of both \mathcal{L} and \mathcal{L}^{mx} depends on the noise model (See Eq.(11) and Eq.(33) of [19]), we use the analytic expressions to compute the FAP of \mathcal{L} and \mathcal{L}^{mx} for Gaussian noise model and different thresholds. The corresponding DP is computed numerically by counting the number of times the statistic crosses a given threshold.

Figure 4 shows the ROC curves of \mathcal{L} and \mathcal{L}^{mx} for LH, LHV, LHVK and LHVKI detector networks which act as representative 2, 3, 4 and 5 detector networks. We see clearly that the ROC curves for \mathcal{L}^{mx} (dashed line) are above that of the \mathcal{L} (solid curve). This means that for a given FAP, the DP of \mathcal{L} is higher than that of \mathcal{L}^{mx} showing better injection recovery.

Network	% of Injections recovered		% fractional improvement of \mathcal{L}^{mx} over \mathcal{L}
	\mathcal{L}	\mathcal{L}^{mx}	
LH	33.59 (45.19)	36.29 (48.52)	8.04 (7.37)
LI	34.79 (47.21)	37.01 (50.51)	6.38 (6.99)
KI	35.00 (47.62)	37.62 (51.09)	7.49 (7.29)
VI	34.84 (47.34)	37.48 (50.81)	7.58 (7.33)
HI	35.50 (48.58)	37.94 (52.01)	6.87 (7.06)
HK	35.83 (48.78)	38.58 (52.43)	7.67 (7.48)
LV	35.62 (48.66)	38.35 (48.66)	7.66 (7.77)
VK	35.75 (48.75)	38.43 (52.36)	7.50 (7.40)
LK	35.88 (49.20)	38.55 (53.93)	7.44 (9.61)
HV	36.06 (49.24)	38.53 (52.72)	6.85 (7.07)
LHI	48.84 (64.58)	50.97 (67.59)	4.36 (4.66)
LKI	50.67 (67.49)	52.87 (70.78)	4.34 (4.87)
LHV	50.02 (66.32)	52.33 (69.48)	4.62 (4.76)
LHK	49.90 (66.11)	52.36 (69.22)	4.93 (4.70)
LVI	50.43 (67.15)	52.45 (70.18)	4.00 (4.51)
HKI	51.11 (68.01)	53.48 (71.25)	4.64 (4.76)
VKI	50.96 (67.73)	53.51 (71.07)	5.00 (4.93)
HVI	51.19 (68.17)	53.36 (71.26)	4.24 (4.53)
HVK	52.11 (69.91)	54.41 (73.26)	4.41 (4.79)
LVK	52.61 (70.44)	54.88 (73.79)	4.31 (4.77)
LHKI	61.55 (79.30)	63.08 (81.70)	2.49 (3.03)
LHVI	61.55 (79.32)	63.03 (81.72)	2.40 (3.03)
LHVK	62.65 (81.29)	64.35 (83.79)	2.71 (3.07)
LVKI	62.85 (81.29)	64.29 (83.70)	2.29 (2.96)
HVKI	63.24 (81.85)	64.89 (84.29)	2.61 (2.98)
LHVKI	70.66 (88.63)	71.50 (90.36)	1.19 (1.95)

TABLE II: Percentage of injections recovered by \mathcal{L} and \mathcal{L}^{mx} for various networks with FAP = 10^{-7} . (2 – 10) M_{\odot} binary injections are sampled uniformly in a volume from sky with source distance varying from $100Mpc$ to $1200Mpc$. $\cos \epsilon$ and Ψ are uniformly sampled from the ranges $(-1, 1)$ and $(0, 360^{\circ})$ respectively. The numbers in bracket denote the percentage of recovered injections in a region with $\epsilon \leq 70^{\circ}$ or $\epsilon \geq 110^{\circ}$. All detectors are assumed with "zero-detuning, high power" Advanced LIGO PSD [26] noise curve.

A. Injection recovery

In Table II, we make quantitative comparison of the performances of \mathcal{L} and \mathcal{L}^{mx} for various networks. We choose the $FAP = 10^{-7}$ for the injection recovery using both \mathcal{L} and \mathcal{L}^{mx} statistics. This corresponds to an SNR threshold of 6.18 for MLR statistic and 5.79 for the *hybrid* statistic. In the second and third columns respectively, we list the percentage of injections recovered by \mathcal{L} and \mathcal{L}^{mx} . In the fourth column, we list the fractional improvement in the injection recovery of \mathcal{L}^{mx} over \mathcal{L} . In all the columns, the (un)bracketed numbers are from (full range) restricted range of ϵ from (sample-1) sample-2.

Variation with the number of detectors: We note that the injection recovery using both \mathcal{L} and \mathcal{L}^{mx} (Columns II and III in Table II) increases with the number of detectors in the network. For the full range of ϵ , the typical average injection recovery using \mathcal{L} (\mathcal{L}^{mx}) is $\sim 35.29\%$ (37.88%), 50.78% (53.06%), 62.37% (63.93%) and 70.66% (71.5%) for 2, 3, 4 and 5 detector networks respectively. This is primarily because the network SNR ρ of a given source increases with the number of detectors, which in turn increases the distance reach as well as detection volume of the network (See Table I - Column IV-V). Thus, successively adding detectors one-by-one in a typical 2-detector network the injection recovery would increase by $\sim 48\%$ for 3, $\sim 86\%$ for 4 and $\sim 110\%$ for 5 detectors with respect to the 2 detector network.

Variation within the fixed number of detectors: For networks with fixed number of detectors, the injection recovery (for both \mathcal{L} and \mathcal{L}^{mx}) increases with the sky coverage of the network listed in Table I (Column III). Amongst the 3 detector networks, LVK and HVK shows the higher values of injection recovery (due to their high sky coverage). Similarly HVKI shows high recovery amongst the 4 detector networks in this exercise. However, though the sky coverage is quite different for LHVI ($\sim 79\%$) as compared to HVKI ($\sim 100\%$), we see only small variation in the injection recovery. This could be because LHVI has longer distance reach than HVKI. Thus, the injection recovery is an interplay of both these effects.

Variation with the choice of inclination angle range: For injections with the restricted binary inclinations *i.e.* sample-2, both \mathcal{L} and \mathcal{L}^{mx} give higher recovery rate compared to the injections in the full range. For example, for the 3 detector network LHI, the injection recovery rate of \mathcal{L} is 48.84% (64.58%) for full (restricted) range. This is because non-spinning binary has higher SNR in the region with ($\epsilon \leq 70^\circ$ or $\epsilon \geq 110^\circ$) for a given sky location and distance as compared to near edge-on region. Therefore, in the restricted region, all the injections are likely to have higher SNR and hence the fraction of injections from this region crossing a given threshold would be always higher than the fraction from the entire region. Hence, the recovery rate of both \mathcal{L} and \mathcal{L}^{mx} improve in the restricted region.

Improvement of injection recovery with \mathcal{L}^{mx} over \mathcal{L} : In Table II (Column IV), we tabulate the percentage fractional improvement in the injection recovery of \mathcal{L}^{mx} compared to \mathcal{L} . The improvement in injection recovery decreases with increase in the number of detectors. This improvement, on an average is $\sim 7.35\%$ (7.54%), $\sim 4.48\%$ (4.73%), $\sim 2.5\%$ (3.01%) and $\sim 1.19\%$ (1.95%) for 2, 3, 4 and 5 detector networks respectively in full (restricted) range of ϵ . As discussed earlier, as the number of detectors increases, the SNR increases and hence the recovery increases for both the statistics and the advantage of \mathcal{L}^{mx} over \mathcal{L} reduces. Thus, it is clear that \mathcal{L}^{mx} is more advantageous for network search with small number of detectors for a given source.

Variation of injection recovery rate with ϵ : The network SNR of the binary signal varies with the inclination angle ϵ . Hence the DP and subsequently the injection recovery rate of

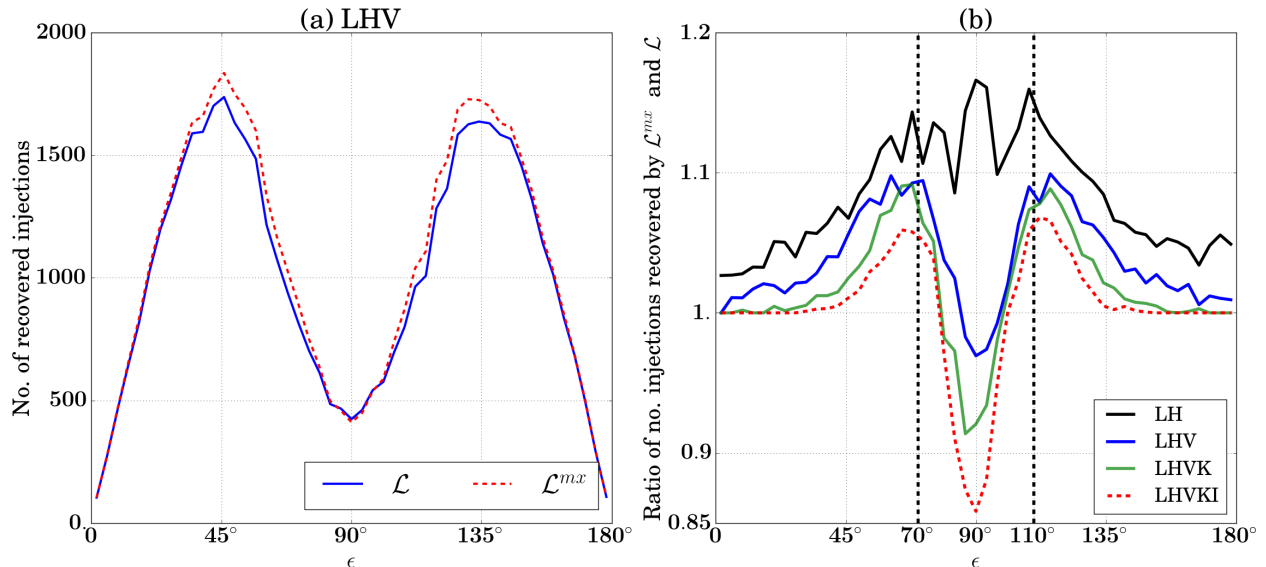


FIG. 5: (a) Histogram of injections recovered by \mathcal{L} (solid curve) and \mathcal{L}^{mx} (dashed curve) along ϵ for the networks LHV for $\mathbf{FAP} = 10^{-7}$. (b) Ratio of number of injections recovered by \mathcal{L}^{mx} and \mathcal{L} along ϵ for various networks. 5×10^5 NS-BH binary injections with masses $(2 - 10)M_{\odot}$ are sampled uniformly from sky with source distance vary from 100Mpc to 1200MPc uniform in volume. $\cos \epsilon$ and Ψ are uniformly sampled from the ranges $(-1, 1)$ and $(0, 360^{\circ})$ respectively.

\mathcal{L} and \mathcal{L}^{mx} changes with ϵ . In Figure (5.a), we draw the histogram of number of recovered injections (for $\mathbf{FAP} = 10^{-7}$) by \mathcal{L} and \mathcal{L}^{mx} with respect to ϵ for a representative network LHV. We note that the histogram follows the trend of the expected distribution of binary inclination angle given in Eq.(28) of [25]. This distribution is obtained by combining SNR information of the binary signal with the uniform prior distribution of $\cos \epsilon$.

If all the other parameters are fixed, the network SNR is maximum for $\epsilon = 0, 180^{\circ}$ (face-on/off) and minimum for $\epsilon = 90^{\circ}$ (edge-on). The injections are sampled with uniform distribution of $\cos \epsilon$, which gives less number of near face-on injections as compared to edge-on. Due to the combined effect of SNR variation and the distribution of injections, the recovered injection follows the distribution in Figure (5.a).

The improvement in the recovered number of injections of \mathcal{L}^{mx} with respect to \mathcal{L} also varies with ϵ . In Figure (5.b), we plot the ratio of number of injections recovered by \mathcal{L}^{mx} and \mathcal{L} for various networks as a function of the ϵ . As ϵ increases from 0, the fractional improvement in injection recovery of \mathcal{L}^{mx} increases steadily till $\epsilon \sim 70^{\circ}$, then it starts falling. As one can see for all networks, near edge-on cases \mathcal{L}^{mx} recover less injections compared to \mathcal{L} . As ϵ increases from face-on cases, the optimum matched filter SNR ρ of the signal decreases. However, for \mathcal{L}^{mx} , the optimum SNR loss is compensated by the reduction in ρ_{th} . Therefore, \mathcal{L}^{mx} recover more injections compared to \mathcal{L} . However, as ϵ crosses $\sim 70^{\circ}$, as described in [19], the fraction of optimum SNR captured by \mathcal{L}^{mx} drops rapidly and can not be compensated by the reduction in threshold. Therefore the performance of \mathcal{L}^{mx} decline near $\epsilon = 90^{\circ}$. A similar effect repeats in the region $\epsilon \geq 90^{\circ}$. However, as we expect less binary sources near edge-on region with appreciable SNR, on average the \mathcal{L}^{mx} gives better performance compared to \mathcal{L} .

VI. CONCLUSION

In this paper we perform a quantitative performance comparison of multi-detector MLR statistic \mathcal{L} and the *hybrid* statistic \mathcal{L}^{mx} for various networks. We compute and compare the signal recovery rates of \mathcal{L} and \mathcal{L}^{mx} for a fixed FAP = 10^{-7} . We further study the variation of injection recovery with the binary inclination angle ϵ .

We have demonstrated the performance by using the noise model as Gaussian with "zero-detuning, high power" Advanced LIGO PSD [26] for the NS-BH system of masses $(2 - 10)M_{\odot}$. The ROC curves are used as a tool for this demonstration. The source location is sampled uniformly from the sky sphere with distance vary between 100Mpc to 1200Mpc. The inclination angle and polarization angle are sampled uniformly from the polarization sphere. ROC curves are generated for representative 2, 3, 4 and 5 detector combinations. On average, the MLR statistic recover $\sim 35.29\%$, 50.78% , 62.37% and 70.66% of injections in 2, 3, 4 and 5 detector networks respectively for a fixed FAP of 10^{-7} . The *hybrid* statistic shows $\sim 7.35\%$, $\sim 4.48\%$, $\sim 2.5\%$ and $\sim 1.19\%$ relative improvement in the injection recovery rate over generic MLR statistic for 2, 3, 4 and 5 detector networks respectively for the same FAP.

The real GW detector noise is not pure Gaussian but is contaminated by the non-Gaussian noise transients namely glitches. Hence for real searches, it is not ideal to use the *hybrid* statistic as defined in Eq.(4.3). One might need to reweigh \mathcal{L}^{mx} by the χ^2 statistic in the similar way demonstrated in [14] for \mathcal{L} .

In this study, all the simulations are carried out for an NS-BH binary system with fixed masses. In real search scenario, the masses are unknown and one needs to place templates in mass space and perform the search. A template-based search increases the false alarms. However, this applies to the search based on both *hybrid* statistic \mathcal{L}^{mx} and the MLR statistic \mathcal{L} and further owing to a single stream, we expect to get less false alarms for *hybrid* statistic as compared to the MLR statistic.

In [27], authors used a face on/off tuned MLR statistic (single stream) for the GW follow-up search of short Gamma Ray Bursts (GRBs) of IPN triggers. This was targeted search with templates in mass parameter space in LIGO-Virgo data. The results did show a similar improvement in the false alarm rates compared to generic MLR statistic as we got for the fixed masses simulations of *hybrid* statistic. The short GRBs are expected to have narrow opening angle ($< 30^{\circ}$). However, in this paper we show that *hybrid* statistic can preform better than the generic MLR statistic for much wider region of inclination angle and hence it can be used for the search of binary inspirals having arbitrary inclination angle without compromising too much on the network SNR.

VII. ACKNOWLEDGMENT

The authors availed with the 128 cores computing facility established by the MPG-DST Max Planck Partner Group at Indian Institute of Science Education and Research Thiruvananthapuram. Vinaya Valsan is supported by INSPIRE program of Department of Science and Technology, India. The authors would like to thank Collin Capano for reviewing the draft and for useful comments. This document has been assigned LIGO laboratory document

number LIGO-P1600331.

-
- [1] Abbott B P *et al.* (Virgo, LIGO Scientific) 2016 *Phys. Rev. Lett.* **116** 061102 (*Preprint* 1602.03837)
 - [2] Abbott B P *et al.* (Virgo, LIGO Scientific) 2016 *Phys. Rev. Lett.* **116** 241103 (*Preprint* 1606.04855)
 - [3] Acernese F *et al.* (VIRGO) 2015 *Class. Quant. Grav.* **32** 024001 (*Preprint* 1408.3978)
 - [4] The Virgo Collaboration 2012 Advanced Virgo Technical Design Report Tech. Rep. VIR-0128A-12 Virgo Collaboration URL <https://tds.virgo-gw.eu/ql/?c=8940>
 - [5] Aso Y, Michimura Y, Somiya K, Ando M, Miyakawa O, Sekiguchi T, Tatsumi D and Yamamoto H (The KAGRA Collaboration) 2013 *Phys. Rev.* **D88**(4) 043007 (*Preprint* 1306.6747)
 - [6] Somiya K 2012 *Class. Quant. Grav.* **29** 124007 (*Preprint* 1111.7185)
 - [7] 2011 Ligo-india, proposal of the consortium for indian initiative in gravitational-wave observations (indigo) Tech. Rep. LIGO-M1100296-v2 LIGO Document Control Center URL <https://dcc.ligo.org/LIGO-M1100296/public>
 - [8] Unnikrishnan C S 2013 *Int. J. Mod. Phys.* **D22** 1341010 (*Preprint* 1510.06059)
 - [9] Abbott B P *et al.* (Virgo, LIGO Scientific) 2016 *Phys. Rev.* **X6** 041015 (*Preprint* 1606.04856)
 - [10] Abbott B P *et al.* (Virgo, LIGO Scientific) 2016 *Astrophys. J.* **833** 1 (*Preprint* 1602.03842)
 - [11] Abbott B P *et al.* (Virgo, LIGO Scientific) 2016 *Astrophys. J.* **832** L21 (*Preprint* 1607.07456)
 - [12] Abadie J *et al.* (VIRGO, LIGO Scientific) 2010 *Class. Quant. Grav.* **27** 173001 (*Preprint* 1003.2480)
 - [13] Pai A, Dhurandhar S and Bose S 2001 *Phys. Rev.* **D64**(4) 042004 (*Preprint* gr-qc/0009078)
 - [14] Harry I W and Fairhurst S 2011 *Phys. Rev.* **D83**(8) 084002 (*Preprint* 1012.4939)
 - [15] Haris K and Pai A 2014 *Phys. Rev.* **D90** 022003 (*Preprint* 1401.7967)
 - [16] Abadie J *et al.* (LIGO Scientific) 2012 *Astrophys. J.* **760** 12 (*Preprint* 1205.2216)
 - [17] Aasi J *et al.* (VIRGO, IPN, LIGO Scientific) 2014 *Phys. Rev. Lett.* **113** 011102 (*Preprint* 1403.6639)
 - [18] Macleod D, Harry I W and Fairhurst S 2016 *Phys. Rev.* **D93**(6) 064004 (*Preprint* 1509.03426)
 - [19] Haris K and Pai A 2016 *Phys. Rev.* **D93**(10) 102002 (*Preprint* 1512.00655)
 - [20] Aasi J *et al.* (LIGO Scientific) 2015 *Class. Quant. Grav.* **32** 074001 (*Preprint* 1411.4547)
 - [21] Harry G M (LIGO Scientific) 2010 *Class. Quant. Grav.* **27** 084006
 - [22] Abbott B P *et al.* (Virgo, LIGO Scientific) 2016 *Phys. Rev. Lett.* **116** 131103 (*Preprint* 1602.03838)
 - [23] Abbott B P *et al.* (LIGO Scientific) 2016 (*Preprint* 1602.03845)
 - [24] Abbott B P *et al.* (Virgo, LIGO Scientific) 2016 *Phys. Rev. Lett.* **116** 241102 (*Preprint* 1602.03840)
 - [25] Schutz B F 2011 *Class. Quant. Grav.* **28** 125023 (*Preprint* 1102.5421)
 - [26] 2010 Advanced LIGO anticipated sensitivity curves Tech. Rep. LIGO-T0900288-v3 LIGO Document Control Center URL <https://dcc.ligo.org/cgi-bin/DocDB/ShowDocument?docid=2974>
 - [27] Williamson A, Biwer C, Fairhurst S, Harry I, Macdonald E, Macleod D and Predoi V 2014 *Phys. Rev.* **D90** 122004 (*Preprint* 1410.6042)